AGU PUBLICATIONS

Geophysical Research Letters

RESEARCH LETTER
10.1002/2014GL061923

**Key Points:**
- GPS-based distributed fault slip model derived in real time for early warning
- Reasonable first order approximation of South Napa slip distribution at $M_w$ 5.9
- $M_w$ 6.0 is resolution limit for current North California rtGPS network and processing

**Supporting Information:**
- Readme
- Movie S1
- Movie S2
- Movie S3
- Movie S4

**Correspondence to:**
R. Grapenthin,
rg@nmt.edu

**Citation:**
Grapenthin, R., I. Johanson, and R. M. Allen (2014), The 2014 $M_w$ 6.0 Napa earthquake, California: Observations from real-time GPS-enhanced earthquake early warning, *Geophys. Res. Lett.*, *41*, doi:10.1002/2014GL061923.

Received 18 SEP 2014
Accepted 07 NOV 2014
Accepted article online 11 NOV 2014

# The 2014 $M_w$ 6.0 Napa earthquake, California: Observations from real-time GPS-enhanced earthquake early warning

**Ronni Grapenthin[1], Ingrid Johanson[2], and Richard M. Allen[2]**

[1]Department of Earth and Environmental Science, New Mexico Institute of Mining and Technology, Socorro, New Mexico, USA, [2]Berkeley Seismological Laboratory, University of California, Berkeley, California, USA

**Abstract** Recently, progress has been made to demonstrate feasibility and benefits of including real-time GPS (rtGPS) in earthquake early warning and rapid response systems. Most concepts, however, have yet to be integrated into operational environments. The Berkeley Seismological Laboratory runs an rtGPS-based finite fault inversion scheme in real time. This system (G-larmS) detected the 2014 $M_w$ 6.0 South Napa earthquake in California. We review G-larmS' performance during this event and 13 aftershocks and present rtGPS observations and real-time modeling results for the main shock. The first distributed slip model and magnitude estimates were available 24 s after the event origin time, which, after optimizations, was reduced to 14 s (≈ 8 s *S* wave travel time, ≈ 6 s data latency). G-larmS' solutions for the aftershocks (that had no measurable surface displacements) demonstrate that, in combination with the seismic early warning magnitude, $M_w$ 6.0 is our current resolution limit.

## 1. Introduction

The importance of including real-time GPS (rtGPS) into earthquake early warning (EEW) systems has been recognized for a few years and found wide acceptance after the 2011 Tohoku-oki earthquake. Much progress has been made to demonstrate the feasibility and benefits of either GPS-only EEW or seismic and GPS EEW integrations [*Crowell et al.*, 2009; *Allen and Ziv*, 2011; *Melgar et al.*, 2012; *Wright et al.*, 2012; *Ohta et al.*, 2012; *Colombelli et al.*, 2013; *Minson et al.*, 2014; *Grapenthin et al.*, 2014]. The biggest contribution GPS brings to seismic *P* wave detection algorithms is the near instantaneous measurement of permanent surface displacements during and after an earthquake. These data can be used to constrain slip on finite faults and hence derive a geodetic magnitude of the event. Tests of proposed concepts rely on simulated real-time replay of either real data from a different location, which implies a different station geometry, or synthetic data, which currently lack the dynamics of real events. Operational real-time analysis, on the other hand, provides the benefits of testing algorithms in their production location with realistic noise and data gaps, data latencies, network resolution, and resource requirements.

The California Integrated Seismic Network ShakeAlert [*Böse et al.*, 2014] is a real-time EEW demonstration system for California. Currently, three algorithms triggering on *P* wave arrivals in seismic data feed event detections into a Decision Module, which combines magnitude, location, and origin time estimates from the algorithms and sends alarms to its subscribers. During this demonstration phase, ShakeAlert subscribers range from users in science and industry to triggered algorithms.

*Grapenthin et al.* [2014] describe a partially triggered, least squares-based rtGPS static offset inversion algorithm (G-larmS), which has been tested in real time at the Berkeley Seismological Laboratory (BSL) since the beginning of May 2014. G-larmS detected the $M_w$=6.0 South Napa earthquake that nucleated on 24 August 2014 at 10:20:44 UTC near Napa, California (Figure 1). The event was recorded by a network of 58 real-time high-rate (1 Hz) GPS stations in the greater San Francisco Bay Area, a combination of stations from the Bay Area Regional Deformation [*BARD*] network, operated by the BSL, the Plate Boundary Observatory (PBO) operated by UNAVCO and those operated by the U.S. Geological Survey (USGS), Menlo Park. The BSL generates real-time displacement time series for a network of these stations (Figure 1) from which G-larmS estimates permanent surface displacements upon receipt of a ShakeAlert to infer a geodetic magnitude for the triggering event.

Here we review the real-time online performance of G-larmS during this event and 13 aftershocks. This sequence provides a unique opportunity to study system performance based on random temporal

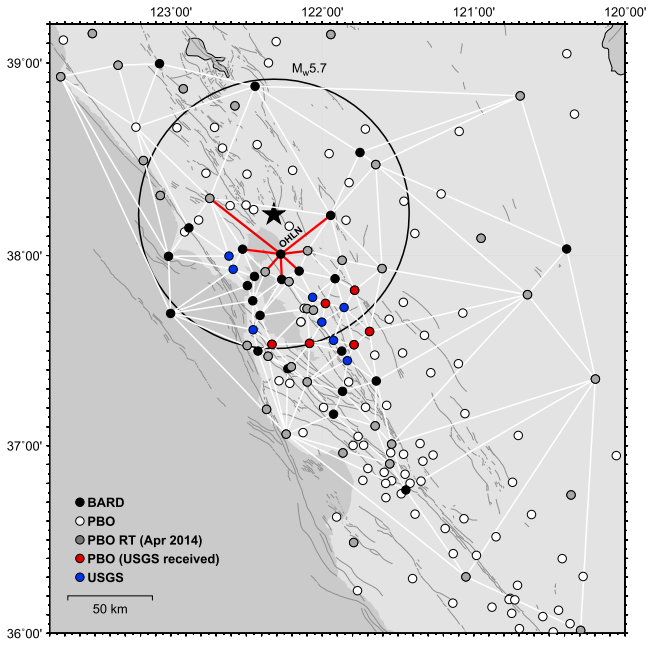


**Figure 1.** Network of high-rate GPS station baselines (dot color indicates operator) in the greater San Francisco Bay Area processed at the BSL. High-rate PBO stations that are not yet real-time capable (as of April 2014) are shown as white dots. Black star marks event epicenter, black circle represents G-larmS' baselines selection area for a $M_w$=5.7 event (78 km radius). OHLN is closest site. Baselines that delivered first offsets are colored red.

sampling but virtually stationary spatial sampling in a real-time environment. We compare the real-time analysis results of the main shock, which induced permanent surface displacements (up to 2.9 cm, six real-time stations within ≈ 25 km of the epicenter show more than 1 cm of permanent displacement (courtesy of Bill Hammond, University of Nevada, Reno; based on GPS processing at Nevada Geodetic Laboratory)) to analyze results for the aftershocks. The aftershocks were too small to induce measurable motion at the surface, which gives us an opportunity to investigate the impact of real-time noise on solution quality.

## 2. Data Analysis

The rtGPS data are streamed into the BSL and analyzed in a network of 169 baselines (Figure 1). For each baseline, one station is assumed static (base station) while the motion of the other site (rover) is given relative to the base station. Positioning solutions for each baseline are generated by individual trackRT processes with ultrarapid (predicted) orbits provided by the International GNSS Service [*Dow et al.*, 2009]. The trackRT software is distributed as part of the GAMIT/GLOBK GPS processing package [*Herring et al.*, 2010]. Further details on the GPS processing are given by *Grapenthin et al.* [2014].

The displacement time series generated by trackRT are streamed into G-larmS, which performs continuous quality analysis on the data. When triggered by ShakeAlert, G-larmS estimates static offsets along the baselines and inverts these for distributed slip on a finite fault from which geodetic magnitude is calculated. ShakeAlert currently consists of several algorithms that generate EEW messages based on *P* wave detection in seismic data. As rtGPS alone is too noisy for *P* wave detection even for large events (e.g., *Ohta et al.* [2012] applies a short-term average/long-term average (STA/LTA) picker to static offset detection for the 2011 Tohoku earthquake), we turn G-larmS into a ShakeAlert subscriber and use the time between alarm receipt and *S* wave arrival to set up the processing (e.g., Green's function generation). Details of the individual processing steps are described by *Grapenthin et al.* [2014], we provide only a summary.

Upon receipt of a ShakeAlert alarm G-larmS is intended to select a subset of baselines within a radius, $r \leq \max(1.5 \times 2^{M_w}, 50)$ (e.g., $r(M_w\ 6.0) = 96$ km), to reduce the processing load ($M_w$ is initial ShakeAlert magnitude). However, in the current test phase G-larmS uses all baselines for all triggering events to test computational resource needs. The circle in Figure 1 encloses stations and associated baselines that would be used in a large production network (e.g., California wide).

G-larmS calculates preevent positions for these baselines by averaging buffered position solutions up to the ShakeAlert event origin time. The estimation of an average postevent position begins with the expected *S* wave arrival at the site of the baseline that is closest to the event. The postevent position is an average over a time window that increases with new data arrivals. Static offsets are the difference of postevent and preevent positions, and are used in a least squares inversion for distributed slip on a finite fault.

In the inversion for slip, we center a vertical 50 km long fault (5 segments, 10 km length each) on the ShakeAlert epicenter. The strike is currently prescribed to be San Andreas Fault parallel (320°N). In width, the fault reaches from the surface to 12 km, the bottom of the seismogenic zone in this region. The analytical expressions for strike slip and dip slip by *Okada* [1985] provide Green's functions. The inversion

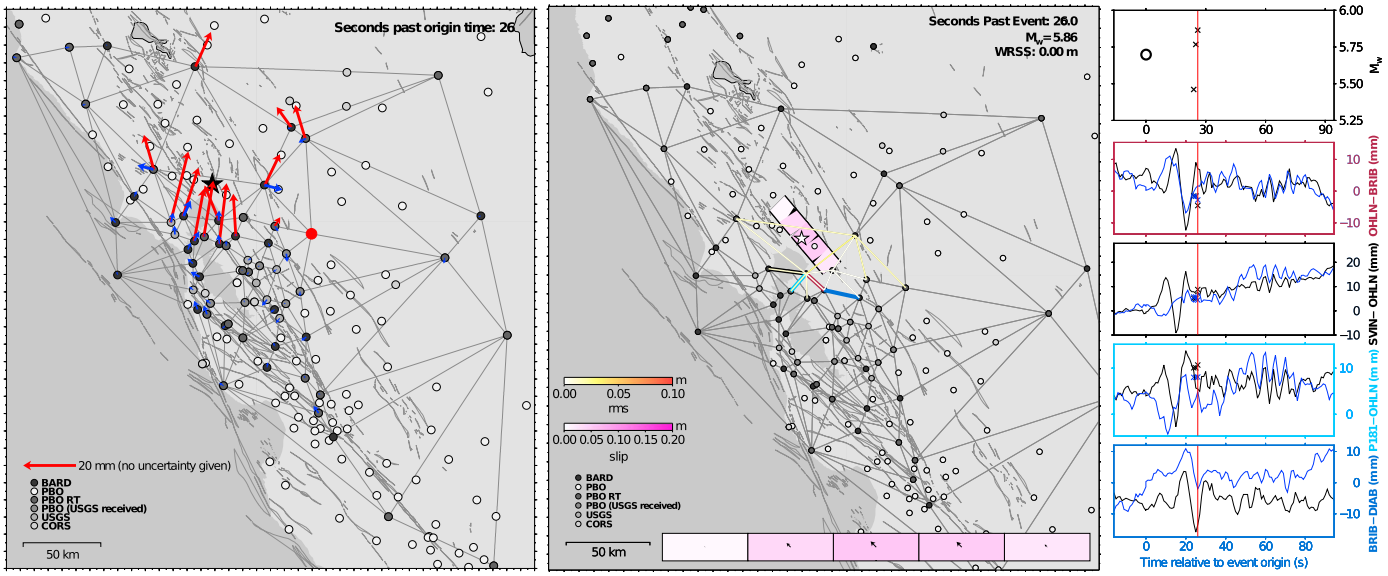


**Figure 2.** Real-time solution produced 26 s after the event origin time (first solution was at 24 s, event location given by black star). (left) Offsets with respect to site P256 (large red dot). Blue offsets are static horizontal offsets from rapid daily time series (courtesy of UNR). Red vectors give real-time offsets from ≈5 min of preevent data and 3 s of postevent data. Real-time data uncertainties are large and omitted. (middle) Model at 26 s after the event using offsets shown as red vectors in the left panel. White to yellow colored baselines indicate model misfit. Projection of vertical fault is shown in map view. Pink colors indicate slip amplitude. N-S (left to right) fault cross section is at the bottom of the panel: vectors give rake (right lateral) normalized to maximum rake of the final solution. (right) Top panel shows time series of GPS-based magnitude, black circle shows initial ShakeAlert magnitude; bottom four panels show north (blue) and east (black) displacement time series for bold, colored baselines in the middle panel. Crosses mark offsets derived along these baselines (time shift between GPS solutions and offsets is due to 6 s data acquisition and processing latency). Movies S1 and S2 in the supporting information animate the time series.

routine (currently no weighting based on solution quality) estimates slip as soon as static offsets are available and repeats at every epoch. The solution is regularized through Laplacian smoothing with a constant smoothing factor.

## 3. Real-Time Results

During the event data from 58 out of 61 real-time stations streamed into the BSL (except P189, P262, and P298). This gives us 159 of 169 baselines with displacement solutions. Problems with sites P189 and P298 were related to the local configuration, which is now corrected. P262 was not operational during a time period that includes this event, which created a hole in our triangulated processing network.

G-larmS received a ShakeAlert trigger at 10:20:49.5 UTC with an estimated event origin time at 10:20:44.4 UTC, a location about 3 km from the location in the Advanced National Seismic System (ANSS) catalog, and an initial magnitude of $M_w$=5.7 ($r$ = 78 km). The station closest to the event origin is OHLN at about 23 km south of the epicenter (Figure 1). Assuming an effective $S$ wave velocity of 3 km/s, the arrival of static offsets was expected at 10:20:52 UTC for baselines involving OHLN (Figure 1). However, G-larmS produced the first static offset estimates and magnitude solutions 16 s later than that (24 s after origin time, 10:21:08 UTC). In addition to 8 s of $S$ wave travel time we observed 6 s of data latency and 10 s of additional latency due to a (now corrected) miscalculation of the wait time for $S$ wave arrival (Figure 2). Much of the data latency is due to local buffering (4 s) in a BKG Ntrip Client [*Weber and Mervart*, 2009] to mediate data loss.

Figure 3 shows the displacement field 85 s after the event onset and hence can be considered "final," i.e., only the large displacements at some sites in the far field (e.g., NW vectors) may still be impacted by dynamic displacements. The maximum real-time static offset estimates range from 1.0 to 2.7 cm (outlier removed, Figure 3 red vectors, some of that might be common-mode signal). As we would expect for real-time data and the size of this event, these are overestimates compared to postprocessed daily positioning solutions at these sites (compare blue and red vectors in Figures 2 (dynamic) and 3 (static in near field)). Real-time displacements (red vectors) in Figure 3 mostly agree with postprocessed results (blue vectors, based on 2 days of postevent data) in azimuth (Movie S1 in the supporting information animates displacement field evolution). At that time the amplitudes in the near field have already decreased significantly from those in

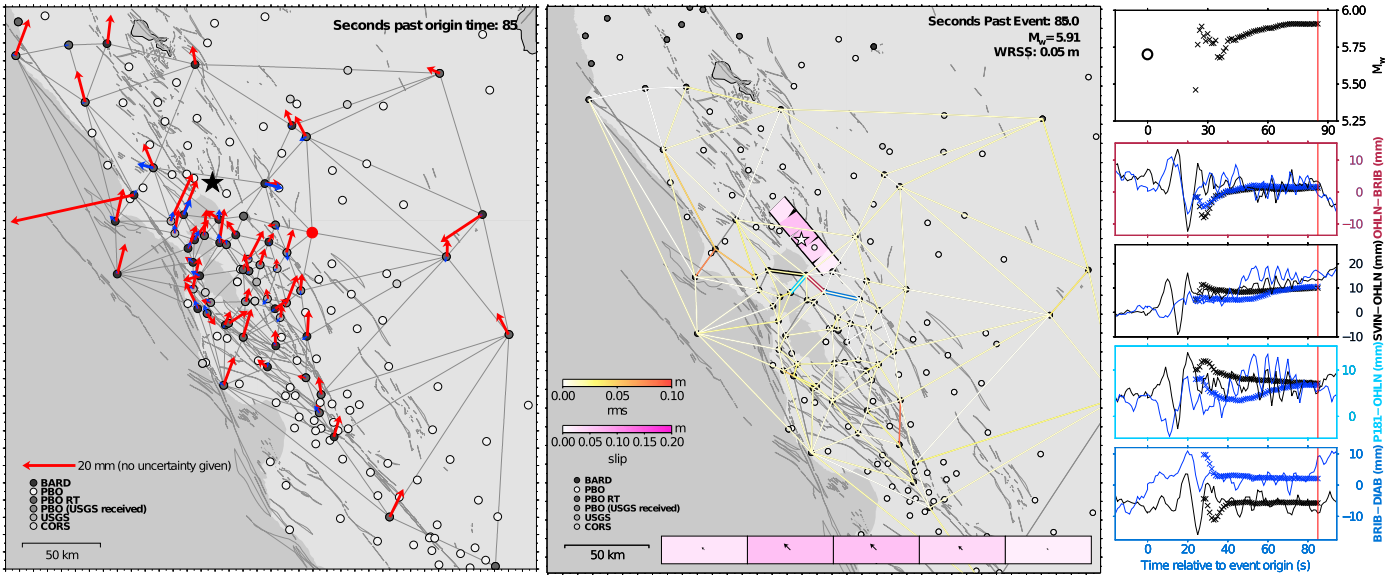


**Figure 3.** Same as Figure 2 but showing "final" real-time solution 85 s past event origin. Large outlier pointing west is station MCCM (poor-sky view). Movies S1 and S2 in the supporting information animate the time series.

Figure 2 but are still overestimates compared to the postprocessed results. The time series in Figure 3 (right) show this more clearly. The offset estimation begins during the last phase of the dynamic displacements, resulting in an initially much larger amplitude which gets averaged out over about 10–15 s. The magnitude time series fluctuates accordingly.

Figures 2 and 3 (middle) show the finite fault slip model and the fit of its predictions to the data at, respectively, 26 and 85 s past the event origin time. The maximum slip during this time is 6.1 cm. The slip maximum first gets pulled toward the south, where we have the initial observations to constrain the model. Toward the end of the process, maximum slip is assigned to a fault patch slightly more north of the epicenter. The time series of the magnitude estimate is shown in Figure 3 (top right). We see slight variations in estimated magnitude at the beginning due dynamic shaking. The median over the first 60 s of solutions is $M_w$=5.86 with a generally good fit to the data (weighted residual sum of squares (WRSS) = 0.05 m, Figure 3).

## 4. Event Replay Results

The bug-related wait time during the real-time analysis prevents us from analyzing the impact of dynamic motion on the real-time solutions. To gain an understanding of what can be expected for such events, we replayed true real-time displacements through G-larmS in simulated real time. A debugged version of G-larmS estimated static offsets and slip models just like in real time but only for baselines within our magnitude-based selection area (Figure 1). The simulation does not add real-time latencies, so 6 s should be added to time values in offset and magnitude time series to approximate real-time scenario (given in parenthesis below).

Figure 4 shows estimated offsets, slip model, and magnitude 16 (22) s and 78 (84) s after the event origin time (time series animations in Movies S3 and S4 in the supporting information). These times correspond roughly to times in Figures 2 and 3. The displacement time series in Figures 2 and 3 (right) clearly show dynamic motion due to *S* wave and surface waves. While the dynamic motion causes overestimates of static offsets, they are damped quickly (≈ 10 s). The maximum magnitude is $M_w$ 6.18 with maximum slip of 17 cm during dynamic motion. The impact of the dynamic motion on the magnitude decays at about 27 s (33 s) after the event onset when the magnitude reaches $M_w$ 5.99 and decays slightly from there. Similar to the real-time results, the final slip model shows most of the high slip on patches slightly to the north and at the epicenter and gives a good fit to the observations.

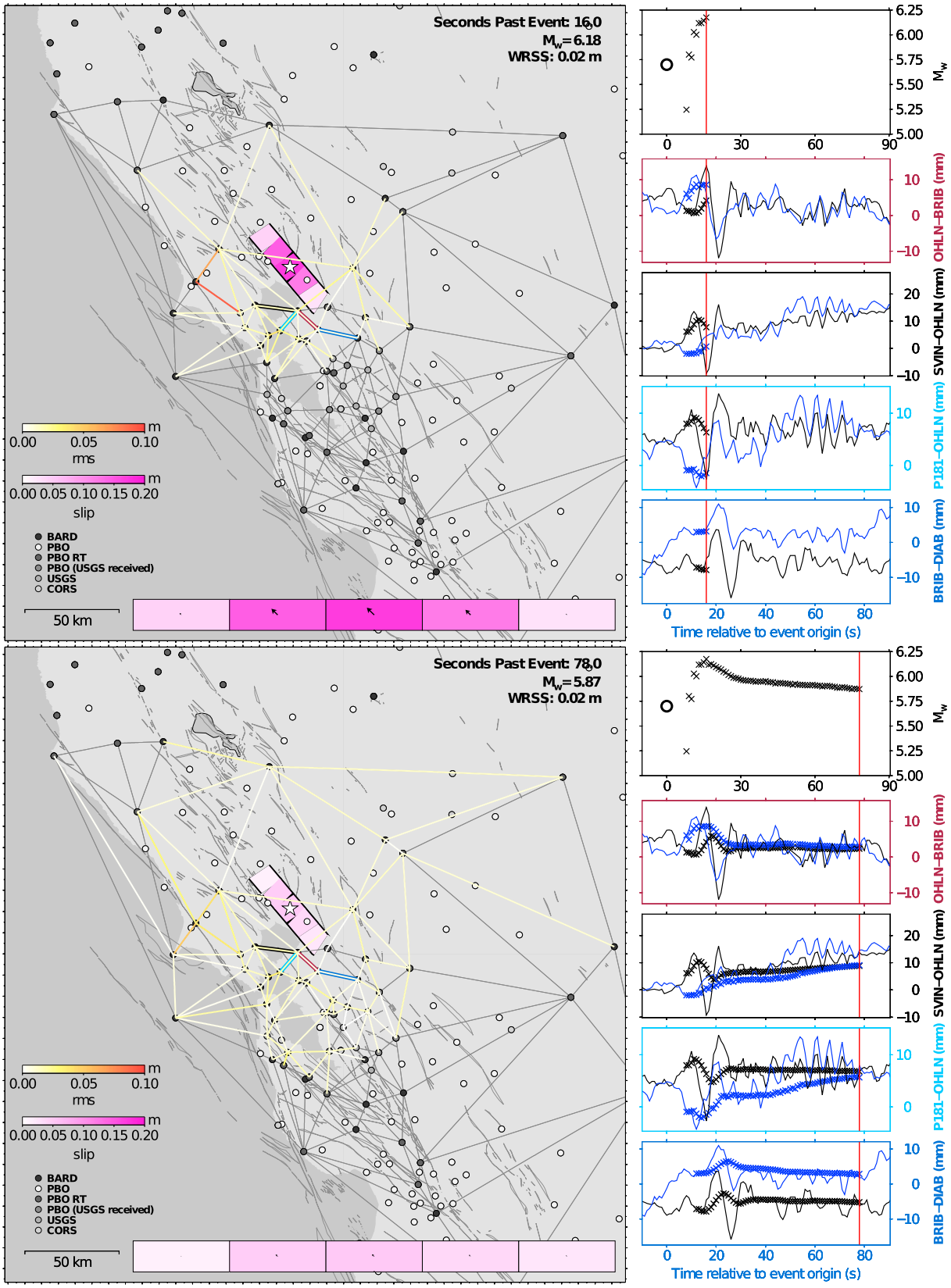


**Figure 4.** Replay of rtGPS solutions in simulated real time with corrected time handling. Snapshots at 16 and 78 s after the event origin time. Figure setup similar to Figures 2 and 3. When started at predicted *S* wave arrival time, the impact of dynamic shaking on the slip model becomes obvious. Offset estimation and magnitudes stabilize after about 10 s.

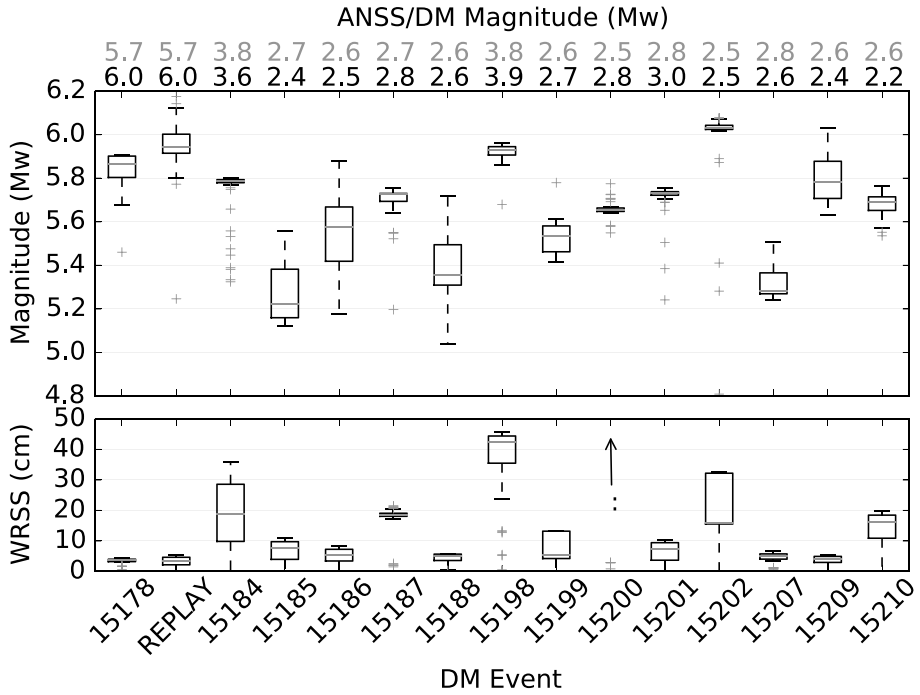


**Figure 5.** G-larmS results for $M_w$=6.0 main shock processed in real time (15178) and replayed (REPLAY), and 13 aftershocks identified by ShakeAlert ID. Each box includes the first 60 results G-larmS produced for each event. (top) Range of inferred magnitudes. (bottom) Misfit of slip model (weighted residual sum of squares). Line in each box is median, boxes extend from 25th to 75th percentile, whiskers cover 1.5 times interquartile range, outliers are plotted individually. Vertical arrow in WRSS panel for event 15200 indicates that misfit is large (median ≈140 cm). ANSS (black) and ShakeAlert (gray) magnitudes for each event are given on the upper horizontal axis.

## 5. Discussion

ShakeAlert did an excellent job alerting for this event: 5.1 s after the origin time an alert was issued, which delivered, for example, a 5 s *S* wave alert time at the BSL. ShakeAlert's initial magnitude estimate was $M_w$ 5.7, which briefly dropped to $M_w$ 5.4 and then stabilized at $M_w$ 5.8–6.0. The point source approximation inherent to seismic algorithms holds for events of this size, and finite source solutions are usually not required. Hence, the South Napa earthquake was an excellent test case for our system, and the seismic results provide validation.

The real-time (and replay) observations show permanent offsets induced by the earthquake in the displacement time series. However, when extracted, these static offsets are slight overestimates in most places; especially at the beginning of the magnitude estimation (compare Figures 2 and 3 (left)). As this still leads to reasonable magnitude estimates, mostly due to large fault surface area over which slip can be smoothed, it motivates the question on how our results for the South Napa earthquake compare to inversions of background noise.

Figure 5 shows the spread of magnitude estimates over the first 60 solutions for the real-time (151878) and replay (REPLAY) events and some of the aftershocks ($M_w$ 2.2–3.9, ShakeAlert IDs 15184–15210) until 29 August. It is obvious that an $M_w$ 6.0 event at the given distance (23 km) is at the lower limit of resolution of our current setup for the region. The magnitude estimates for the aftershocks shown in Figure 5 are based solely on noise in the real-time positioning solutions (ANSS magnitudes given in black on top of the horizontal axis, real-time ShakeAlert magnitudes given above that in gray). The medians for most events range between $M_w$ 5.2 and 5.8 with two events at $M_w$ 5.9 and $M_w$ 6.0. Clearly, the seismic system gives very reliable solutions in this magnitude range and is the primary way to decide whether G-larmS should send out an alarm. The final G-larmS production setup will send out magnitudes only if the seismic magnitude is greater than ≈5.5. Another means to automatically evaluate solution quality is the model misfit (here: weighted residual sum of squares, WRSS). High-magnitude estimates for noisy data should give higher misfit of model

predictions, but exceptions exist (event 15209). Generally, these observations suggest that the solutions for the $M_w$ 6.0 Napa earthquake are reasonable and not solely based on noise in the network (compare WRSS).

The replay of the event, including code changes and exclusion of far field data fares only slightly better than the original event (15178). Some of the outliers at the high-magnitude range are created during the time dynamic displacements traverse the network. This is inevitable and corrects itself quickly; the overestimates are still within ±0.3 magnitude units, which is a reasonable goal for EEW applications. Implementing a low-pass filter to correct for the impact of dynamic motion would result in longer build-up times to the final magnitude [e.g., *Melgar et al.*, 2012].

During this sequence G-larmS had to process multiple alarms simultaneously and demonstrated that rapid foreshock-aftershock sequences and near-simultaneous, independent events (e.g., Northern California and Southern California) are handled well. However, additional work is required to ensure each event has well defined preevent and postevent positions (currently the entire buffer is averaged, which ignores cases of multiple discrete static offset accumulations due to multiple earthquakes in rapid sequence). Furthermore, G-larmS depends on seismic detection which caused problems during aftershocks of the 2011 Tohoku earthquake [*Ohta et al.*, 2014] and may require implementation of rtGPS-based offset detection algorithms [e.g., *Allen and Ziv*, 2011; *Ohta et al.*, 2012].

A comparison of the real-time slip model to postprocessed slip models, which are available in the hours to weeks after an event, must be very qualitative for two reasons: (1) the available data are inherently different: not all GPS in this region transmit data in real time, and postprocessed GPS data are generally more precise (final orbit estimates are available, multiple iterations for parameter estimation are possible); InSAR data are not available in real time, and (2) real-time inversions operate under tight time constraints, which limit the level of detail of parameter space exploration. Postprocessed slip models (http://comcat.cr.usgs.gov/earthquakes/eventpage/nc72282711#scientific_finite-fault, seismic: Doug Dreger, UC Berkeley; GPS+InSAR: William Barnhart, USGS) put most of the slip of up to 1–1.2 m on small regions up to 10 km north of the epicenter. While our final solutions also put the bulk of the slip north of the epicenter (Figure 3, middle), the fault patches are each 10 km long and Laplacian smoothing distributes the slip to the adjacent patches. Having the initial slip mostly south of the epicenter (Figure 2) is due to a bias in data distribution: early data are from that region. Due to the size of our patches (10 km long, 12 km wide), our peak slip of 6.1 cm is much smaller than those of postprocessed models as it is integrated over a much larger area. Given our coarse discretization, our peak slip location gives a first order approximation of the more refined postprocessed models.

## 6. Summary and Conclusions

We present rtGPS observations and real-time modeling results for the $M_w$ 6.0 Napa earthquake that occurred on 24 August 2014 in Northern California. Almost all aspects of the G-larmS system running at the BSL worked as expected and produced finite fault slip models in real time. A bug in the handling of time in the code caused a delay of 10 s before the first results were produced (additional to 6 s data latency). Due to this the real-time system provided first results 24 s after the origin time (8 s is the estimated *S* wave travel time). We show in a simulated real-time solution that this time can be reduced to 14 s (*S* wave wait time plus data latency, virtually no delay inside G-larmS). As ≈4 s of the 6 s latency are due to data buffering, we will explore in the near future how much this wait time can be reduced while still providing high data completeness.

The magnitudes produced in real time and in replay mode capture the event well, and a first-order distributed slip model is produced. When compared to background noise it is obvious that displacements induced by this event just barely stand out above the noise in this network. The model fit to the data provides an additional metric to automatically evaluate the rtGPS solution quality for $M_w$ ≈6.0 estimates. For the future, this means G-larmS will only publish solutions for events with a ShakeAlert magnitude greater than $M_w$ ≈5.5. Aggregator algorithms like the Decision Module should implement a magnitude threshold at which they consider an rtGPS contribution relevant.

The assumption of fixing the geometry to San Andreas Fault parallel worked well in this case, but work is required to parallelize the solution algorithm and test additional strike and slip orientations in real time. If fully parallelized, this should not add much to the actual solution time as only picking of the best solution of many is required.

In summary, this was an excellent test for the G-larmS implementation at the BSL. The system ran stably, produced the first real-time finite fault slip distributions during an earthquake, and was able to process multiple events in parallel. Observing the many aftershocks and investigating the solutions gives a clear picture on the rtGPS threshold, considering the station-event geometry, on the lower end of the magnitude spectrum in the Bay Area at $M_w \approx 6.0$.

**Acknowledgments**

Some rtGPS data are provided by the Plate Boundary Observatory operated by UNAVCO for EarthScope and supported by NSF (EAR-0350028 and EAR-0732947). Static offsets from data processed at the Nevada Geodetic Laboratory are courtesy of Bill Hammond, UNR, (http://geodesy.unr.edu/billhammond/earthquakes/nc72282711/offsets_24hr_2days.txt). Figures 1–4 were made with GMT [*Wessel and Smith*, 1995], Figure 5 with matplotlib [*Hunter*, 2007]. Data used in this study, including G-larmS code, are available from the authors. This work was funded by the Gordon and Betty Moore Foundation through grant GBMF3024 to UC Berkeley, and the USGS/National Earthquake Hazards Reduction Program award G12AC20348. We thank Jessica Murray and an anonymous reviewer for their constructive comments that improved the manuscript.

Andrew Newman thanks Brendan Crowell and Jessica Murray for their assistance in evaluating this paper.

## References

Allen, R. M., and A. Ziv (2011), Application of real-time GPS to earthquake early warning, *Geophys. Res. Lett.*, *38*, L16310, doi:10.1029/2011GL047947.

BARD, *Data for this study come from the Bay Area Regional Deformation Network (BARD), operated by the UC Berkeley Seismological Laboratory, which is archived at the Northern California Earthquake Data Center (NCEDC)*, doi:10.7932/BARD.

Böse, M., et al. (2014), Early warning for geological disasters, in *Early Warning for Geological Disasters, Adv. Tech. in Earth Sci.*, edited by F. Wenzel and J. Zschau, chap. 3, pp. 49–69, Springer, Berlin, Heidelberg, doi:10.1007/978-3-642-12233-0.

Colombelli, S., R. M. Allen, and A. Zollo (2013), Application of real-time GPS to earthquake early warning in subduction and strike-slip environments, *J. Geophys. Res. Solid Earth*, *118*(7), 3448–3461, doi:10.1002/jgrb.50242.

Crowell, B. W., Y. Bock, and M. B. Squibb (2009), Demonstration of earthquake early warning using total displacement waveforms from real-time GPS networks, *Seismol. Res. Lett.*, *80*(5), 772–782, doi:10.1785/gssrl.80.5.772.

Dow, J. M., R. E. Neilan, and C. Rizos (2009), The international GNSS service in a changing landscape of Global Navigation Satellite Systems, *J. Geod.*, *83*, 191–198, doi:10.1007/s00190-008-0300-3.

Grapenthin, R., I. A. Johanson, and R. M. Allen (2014), Operational real-time GPS-enhanced earthquake early warning, *J. Geophys. Res. Solid Earth*, *119*, 7944–7965, doi:10.1002/2014JB011400.

Herring, T. A., R. W. King, and S. C. McClusky (2010), *GAMIT/GLOBK Reference Manuals Release 10.4,* Mass. Inst. of Technol, Cambridge.

Hunter, J. D. (2007), Matplotlib: A 2D graphics environment, *Comput. Sci. Eng.*, *9*(3), 90–95.

Melgar, D., Y. Bock, and B. W. Crowell (2012), Real-time centroid moment tensor determination for large earthquakes from local and regional displacement records, *Geophys. J. Int.*, *188*(2), 703–718, doi:10.1111/j.1365-246X.2011.05297.x.

Minson, S. E., J. R. Murray, J. O. Langbein, and J. S. Gomberg (2014), Real-time inversions for finite fault slip models and rupture geometry based on high-rate GPS data, *J. Geophys. Res. Solid Earth*, *119*, 3201–3231, doi:10.1002/2013JB010622.

Ohta, Y., et al. (2012), Quasi real-time fault model estimation for near-field tsunami forecasting based on RTK-GPS analysis: Application to the 2011 Tohoku-Oki earthquake ($M_W$ 9.0), *J. Geophys. Res.*, *117*, B02311, doi:10.1029/2011JB008750.

Ohta, Y., T. Kobayashi, R. Hino, T. Demachi, and S. Miura (2014), Rapid coseismic fault determination of consecutive large interplate earthquakes: The 2011 Tohoku-Oki sequence, in *International Association of Geodesy Symposia,* in press.

Okada, Y. (1985), Surface deformation due to shear and tensile faults in a half-space, *Bull. Seismol. Soc. Am.*, *75*, 1135–1154.

Weber, G., and L. Mervart (2009), *The BKG Ntrip Client (BNC)*. Report on EUREF Symposium 2007 in London, Mitteilungen des Bundesamtes fuer Kartographie und Geodaesie, Band 42, Frankfurt, Germany.

Wessel, P., and W. H. F. Smith (1995), New version of the Generic Mapping Tools released, *Eos Trans. AGU*, *76*(33), 329, doi:10.1029/95EO00198.

Wright, T. J., N. Houlié, M. Hildyard, and T. Iwabuchi (2012), Real-time, reliable magnitudes for large earthquakes from 1 Hz GPS precise point positioning: The 2011 Tohoku-Oki (Japan) earthquake, *Geophys. Res. Let.*, *39*, L12302, doi:10.1029/2012GL051894.